NATIONAL AERONAUTICS AND SPACE ADMINISTRATION

Technical Memorandum 33-492

A Fiber Optics Slit System Used for Time-Resolved Diagnostics in a Transient Plasma

George H. Stickford, Jr.

JET PROPULSION LABORATORY
CALIFORNIA INSTITUTE OF TECHNOLOGY
PASADENA, CALIFORNIA

September 15, 1971

NATIONAL AERONAUTICS AND SPACE ADMINISTRATION

Technical Memorandum 33-492

A Fiber Optics Slit System Used for Time-Resolved Diagnostics in a Transient Plasma

George H. Stickford, Jr.

JET PROPULSION LABORATORY
CALIFORNIA INSTITUTE OF TECHNOLOGY
PASADENA, CALIFORNIA

September 15, 1971

PRECEDING PAGE BLANK NOT FILMED

PREFACE

The work described in this report was performed by the Environmental Sciences Division of the Jet Propulsion Laboratory.

ACKNOWLEDGMENTS

The author wishes to thank R. Lee, R. Chapman, and G. Advey, of the JPL Hypervelocity Laboratory, for their assistance on this project. A particular thanks is extended to C. Tuttle for his help in setting up the test and obtaining the experimental results.

CONTENTS

CONTENTS (contd)

ABSTRACT

Through the use of fiber optics, a series of very narrow slits has been constructed and placed at the exit plane of a spectrograph. Plasma radiation dispersed by the spectrograph is incident on the slits and is transmitted to separate phototubes via the quartz fibers. With this technique, time-resolved measurements of the spectral shape of the hydrogen Hβ line have been made and used to determine the electron density of a transient plasma. With some knowledge of the pressure or density, the measurements also give the plasma temperature. Data obtained indicated that the thermodynamic conditions behind the reflected shock in a mixture of 20% H_2-80% He, at incident shock speeds of 12 to 14 km/s and pressures of 66.6 to 133.3 N/m^2 (0.5 to 1.0 mm Hg), correspond to theoretically predicted conditions. Immediately behind the incident shock at speeds of 17 to 24 km/s, the plasma reached equilibrium, then demonstrated a drop in intensity which has been attributed to radiative cooling. At 27 km/s, the data indicated that the plasma did not reach equilibrium, presumably because the plasma cooled within the response time of the phototube intensity measurement.

I. INTRODUCTION

In conducting experimental studies with high-temperature plasmas, it is often more difficult to specify the thermodynamic and thermochemical conditions of the plasma than to make the necessary experimental measurements. In general, one is required to determine the temperature, the pressure or bulk density, and the electron density. If the plasma is not in local thermodynamic equilibrium, one must also specify the heavy particle temperature. In transient plasmas, with which this report deals, the problem is further complicated by the fact that the measurements must be made over a time period of a few microseconds.

There are many standard methods of measuring plasma properties; a good summary is given in Ref. 1. These techniques rely on the specific characteristics of the radiative spectra emitted by the plasma. By carefully monitoring the emitted spectra it is possible to determine all the properties needed to completely specify the thermodynamic and thermochemical conditions of the plasma.

This report describes a new technique for making electron density measurements in transient plasmas through the use of a fiber optics slit system. One can also obtain the temperature if the pressure or density is known. Results are presented which demonstrate the effectiveness and the overall accuracy of the technique.

II. DETERMINATION OF HYDROGEN Hβ LINE SHAPE

A. Computation of Shape

The presence of electrons and ions in a plasma has a large effect on the discrete or line emission from bound-bound atomic transitions. Stark broadening of the lines, due to electron and ion collisions, is the dominant broadening mechanism in singly ionized plasmas (10,000 to 20,000 K); such broadening is strongly dependent on the electron density and nearly independent of the temperature. Thus it is an excellent monitor of the electron density.

Stark broadened line profiles for hydrogen have been computed by Griem, Kolb, and Shen (Ref. 2) and are tabulated by Griem (Ref. 1). An estimate of the theoretical accuracy is placed at 15%. However, a later experiment by Hill and Gerardo (Ref. 3) suggests that the profile for the Hβ line may be much better. Their measured profiles agreed to within ±2% of the calculated profiles.

The Hβ profile is probably the best known spectral indicator of the electron density. For this reason, together with the fact that this line is located in a favorable position of the spectrum, it was decided to concentrate on making time-resolved Hβ profile measurements. Furthermore, if one at the same time obtains absolute intensity measurements of the profile, it is possible to deduce the temperature of the plasma as well.

The procedure used in this study is an iterative one in which the line profile is experimentally measured and the theoretical profile is computed assuming a temperature and electron density. The assumed properties are varied until the calculated line shape matches the measured shape. The matching criterion used is a least squares fit between the measured points and the computed points.

Following Griem (Ref. 1), the line shape is given by

$$L_\lambda = \frac{S(\alpha)}{F_0} \qquad (1)$$

where

$$F_0 = \frac{2.61e}{4\pi\epsilon_0}(Ne)^{2/3} = 1.253 \times 10^{-9}(Ne)^{2/3}$$

is the field strength for singly charged ions, and Ne is the electron density in cm^{-3}. For an isothermal plasma of depth X, in centimeters, the spectrally emitted line intensity is

$$I_\lambda(X) = B_\lambda\left(1 - e^{-SL_\lambda X}\right) \qquad (2)$$

where the line strength S, in consistent units, is

$$S = 0.8834 \times 10^{-12}\lambda_0^2 g_\ell f_{\ell u}\left(\frac{Na}{Q(T)}\right)$$

$$\times \left[e^{-E_u/kT}\left(e^{hc/\lambda_0 kT} - 1\right)\right]$$

The line center wave length λ_0 is in micrometers, the atom number density Na is in cm^{-3}; g_ℓ is the lower level statistical weight, $f_{\ell u}$ is the absorption oscillator strength, Q(T) is the partition function, and E_u is the upper level energy.

The line shape parameter $S(\alpha)$ is tabulated in Ref. 1 at 19 wavelength points from the line center out to a point where the intensity drops to about 1/20 of the line center intensity. Shapes are given for four temperatures (5000, 10,000, 20,000, and 40,000 K) and four electron densities (10^{14}, 10^{15}, 10^{16}, and 10^{17} cm^{-3}). For intermediate values, an interpolation scheme was used whereby the table was interpolated linearly between the listed temperatures and logarithmically between listed electron densities.

Some typical Hβ profiles are shown in Fig. 1. The calculations presented account for reabsorption, although this effect is never greater than 10% of the emitted intensity. Emission from other sources such as the continuum processes and the extended wings of other lines was neglected since these sources contribute less than 1% to the line intensity.

B. Techniques for Measuring Line Shape

There are two basically different techniques for recording the spectrally dispersed radiative intensity emitted by a plasma. The first is a photographic technique in which the photosensitive film is placed in the exit plane of a spectrograph and records all the details of the spectrally resolved radiation. This method is ideally suited to obtaining narrow line profiles of steady state plasma sources; however, for transient plasmas, one requires time-resolved measurements. These can be provided by fast-acting shutters or by translating film cameras. In either case the time resolution is never better than 5 to 10 μs. Furthermore, it is very difficult to obtain absolute intensity measurements using this technique. For these reasons the photographic technique is not well suited to the problem at hand, that is, measuring spectrally resolved and time-resolved (to better than 1 μs) Hβ line profiles.

The second technique commonly used is one in which an electronic photomultiplier tube is placed behind a narrow slit in the exit plane of a spectrograph. The response time of the phototubes and the associated circuitry can be as low as 0.1 μs; thus this technique is capable of resolving the intensity fluctuations of a transient plasma. In addition, the phototubes can be readily calibrated to measure absolute intensities.

The limitation of this method is a physical one, that is, the problem of placing very narrow slits close enough together to resolve the line shape and still have an independent phototube recording the radiation transmitted through each slit. For example, in a spectrograph with a dispersion of 1.0 nm/mm and using phototubes several centimeters in diameter, one would do well to obtain 10.0 nm wavelength resolution. To measure the Hβ profile, as shown in Fig. 1, requires a resolution of at least 0.2 or 0.3 nm.

C. Fiber Optics Slit System

1. Construction. The required wavelength resolution was obtained by constructing the fiber optics slit system[1] shown in Fig. 2a. The slit system consists of seven slits 0.2 mm wide and spaced every 0.5 mm, as shown in Fig. 2b. The slits are filled with three rows of quartz fibers approximately 75 μm in diameter and 30 cm long. The fibers from each slit are individually bundled and can be optically connected to separate phototubes. Thus each phototube monitors the radiation incident on one of the seven slits, giving a spatial resolution of 0.5 mm.

These slits were placed in the focal plane of a Jarrel Ash Model 75-000 Plane Grating Spectrograph[2] (f/6.3, 0.75 m focal length). The grating is blazed for 0.5μmλ, is ruled to 1200 grooves/mm, and has a reciprocal linear dispersion of approximately 0.9 nmλ/mm (at 0.4861 μmλ).[3] The slit spacing is therefore 0.45 nmλ, with each slit viewing a spectral bandpass of 0.18 nmλ. This configuration gives sufficient resolution to resolve the Hβ profile in plasmas with electron densities of from 10^{16} to 10^{17} electrons/cm^3.

2. Slit Function. The slit function for the fiber-filled slits is much more complicated than the standard slit function for a rectangular slit. Consider the enlarged view of a fiber-filled slit shown in Fig. 3. The circular fibers do not completely fill each slit; thus some of the radiation entering the slit does not reach the phototube. Furthermore, as shown by Fig. 3a, the fiber packing may not be optimum and there may be spaces between the rows. Additional dead space can be caused by broken fibers which are nontransmitting. These can be seen in Fig. 2b.

The slit function describing the present experimental setup has been computed. The details of the computation are presented in Appendix A. The results for the two cases which have been computed, corresponding to the two configurations in Fig. 3, are shown in Fig. 4. These curves are for an entrance slit width of 1/4 the exit slit width.

The slit function for the more tightly packed slit, that is, the overlapping-rows case, is very similar to the familiar trapezoidal-shaped slit function for a rectangular exit slit. However, as the distance between the rows of fibers increases, the function exhibits a three-peaked nature, with the difference between the maxima and minima increasing as the row spacing increases. One would expect the existing slits to correspond more closely to the separate-row case. The quartz fibers have been coated with a dissimilar material in order to optimize their transmission characteristics. Thus it is not possible to have perfectly tight packing, as is shown in Fig. 3b. Furthermore, very close inspection indicates that the rows are somewhat separated and that the spacing shown in Fig. 3a appears to be a good average.

An effort was made to verify this reasoning by measuring the actual slit function for each slit. A narrow line was passed over the slits and the transmitted intensity was recorded on an X-Y plotter. Unfortunately the line used had a natural broadening of 100 μm; thus a comparison between the measured and computed slit functions is difficult to make. The measured slit functions are presented in Fig. 5 for two slits. These results indicate that the fiber rows are somewhat separated. The exact degree of separation can be determined only through a more careful slit function measurement. Nevertheless the results give one confidence in the qualitative accuracy of the slit function analysis.

The measured profiles of Fig. 4 also demonstrate a nonsymmetrical nature due to uneven fiber spacing and broken fibers. In Appendix B is detailed a simplified analysis which approximates the error associated with the nonsymmetrical profiles. The magnitude of the maximum error is given by

$$\text{error} = \frac{1}{3}\,\frac{\dfrac{dI_\xi}{I_0}}{d\xi}\,\frac{df(\xi)}{d\xi}$$

where I_ξ is the spectral line intensity, I_0 is the line center intensity, $f(\xi)$ is the slit function, and ξ is a nondimensional wavelength parameter, which is defined in Appendix B. The maximum error for the existing slits and the Hβ line profile at the conditions of interest was found to be less than 1%. This is well within the experimental error and therefore will be neglected.

3. Effective Aperture Angle of the Slits. For maximum efficiency, the optical fibers must gather and transmit as much of the radiation falling on the slit as possible. The effective aperture angle of the fiber-filled slits must be large enough to accept the cone of rays reflected by the focusing mirror. The exit f/number of the spectrograph is 6.3; thus the slits need an aperture angle greater than

$$\theta = \tan^{-1}\left(\frac{1}{2\ f/\text{number}}\right) = 4.5\ \text{deg}$$

The effective aperture angle of the slits was measured by allowing a beam of parallel rays to fall on the slits. The transmitted intensity was monitored as the incident angle was varied. The intensity was found to drop to half its value as the angle was varied from 0 to 12 deg. Thus the effective aperture angle is large enough to receive all rays incident on the slits at the spectrograph focal plane.

[1]The fiber optics slit system was constructed by the Mosaic Fabrications Division of Bendix Corporation, Sturbridge, Mass.

[2]Jarrel Ash Division, Fisher Scientific, Waltham, Mass.

[3]The symbol λ denotes wavelength measurement.

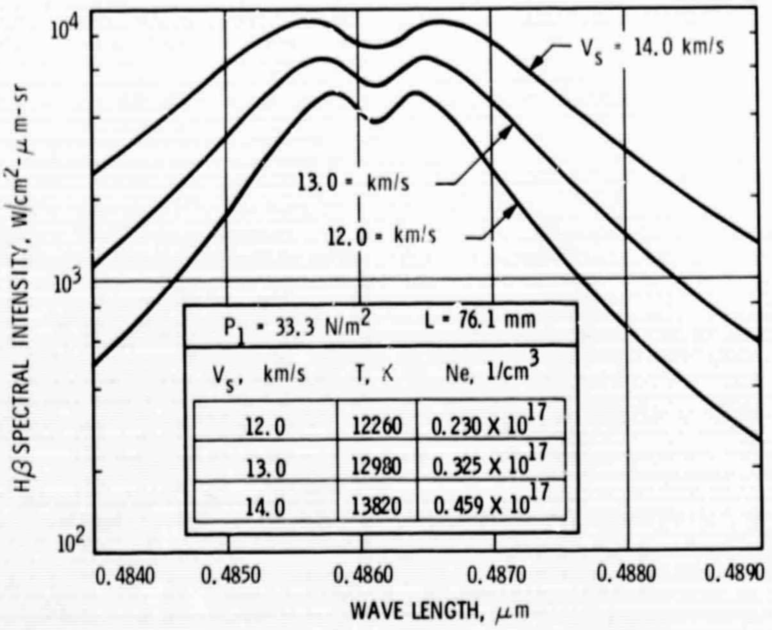

Fig. 1. Spectral intensity emitted by the Hβ line behind a reflected shock wave

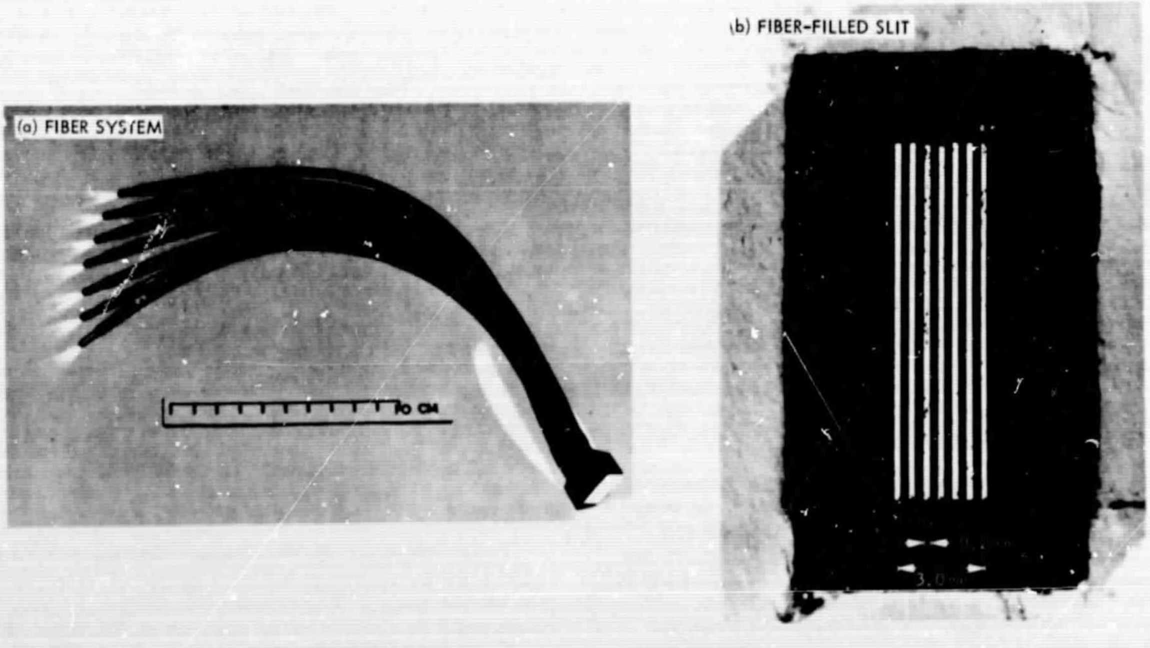

Fig. 2. Photograph of fiber optics slit system

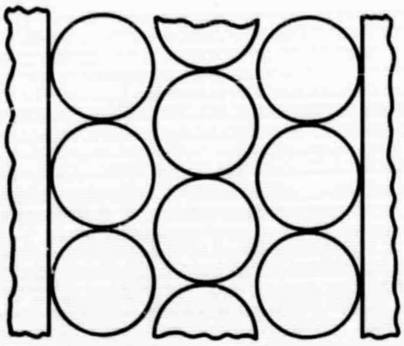

Fig. 3. Schematic of the configuration of fibers in the slits

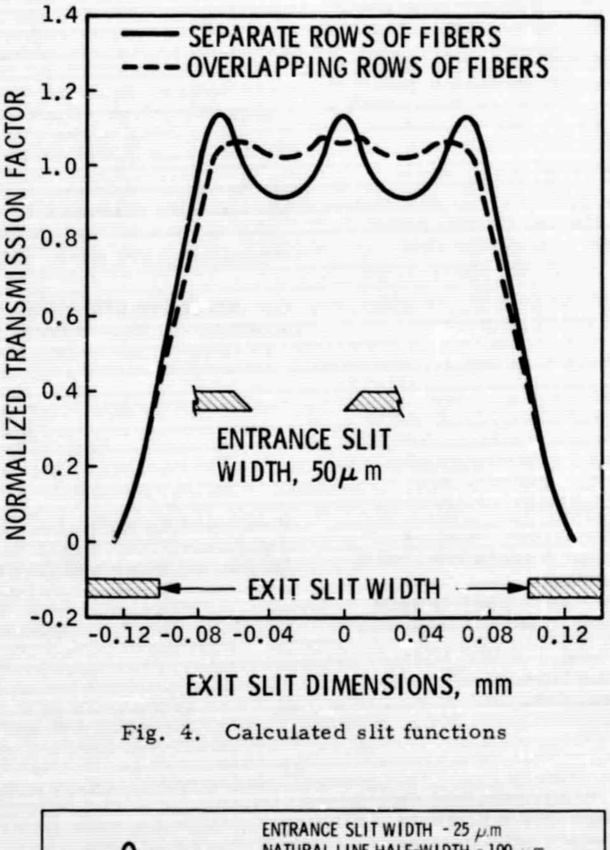

Fig. 4. Calculated slit functions

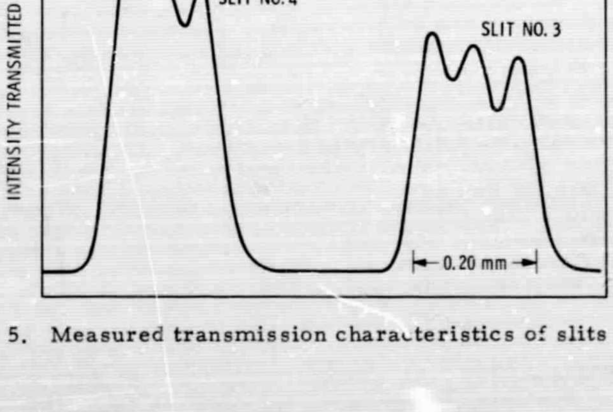

Fig. 5. Measured transmission characteristics of slits 3 and 4

III. EXPERIMENTAL PROCEDURES AND RESULTS

A. Test Setup

The experimental results to be discussed were obtained in the JPL electric-arc-driven shock tube (Ref. 4). A schematic of the experimental setup is shown in Fig. 6. A shock wave is generated by the discharge of an electrical arc in the arc chamber and the subsequent rupture of a thin diaphragm separating the arc chamber and the shock tube. The pressure in the arc chamber before discharge is approximately 10^6 N/m^2 (10 atm); the gas used is helium. Initial pressure in the shock tube ranged from 33.3 to 133.3 N/m^2 (0.25 to 1.0 mm Hg).

The shock velocity and the quality of the flow behind the shock was monitored through collimated slits spaced over the 2-m length of tube just preceding the test port. The 15.2-cm shock tube was 10 m long, and the test port was located 8 m from the diaphragm. The spectrograph was positioned to view a small region of test gas through a quartz window. The volume of test gas viewed was small enough to give better than 0.1 μs time resolution.

In addition to the normal straight-through configuration, the shock tube can be operated in a reflected shock mode by positioning an end plate several millimeters behind the test port. The spectrograph thus views the reflected shock region. With an optical stop placed on the end plate, the length of the test slug viewed could be varied.

The fiber optics slit system was located at the exit plane of the spectrograph (see Fig. 7). Seven RCA 1P28 phototubes were used to monitor the radiation transmitted through the fiber bundles. The phototube power supply and amplifying circuitry are discussed in Ref. 5. The response time of the phototubes and attendant circuitry is normally 0.1 to 0.2 μs; however, due to an error in the phototube circuits, it was discovered that the response time for the measurements to be presented was approximately 1 μs. This is still sufficient response time for all of the present experimental measurements except for one run. The effect of the long response time on this run will be discussed in a later section.

B. Calibration

The calibration of the total system was accomplished by placing a known radiation source at the center of the shock tube. A spectral wavelength calibration was performed by locating known atomic lines produced by a mercury-cadium gas lamp. The accuracy of the calibration was such that the spectral position of the exit slit could be specified to within 0.2 nmλ. The spectral dispersion was found by measuring the physical distance between known lines. The dispersion was found to be 0.900 ± 0.004 nmλ/mm at the Hβ line, 0.4861 μmλ.

An absolute intensity calibration was performed using a carbon arc, which has been shown to be a reliable radiation standard (Ref. 6). Graphite electrodes (National Carbon Co. SPK grade) were burned in a Mole-Richardson[4] lamp at 12.5 A. The electrodes are oriented at a 120-deg included angle. The positive electrode is 6.1 mm in diameter and has a uniform crater approximately 3 mm in diameter.

The intensity emitted by the arc was assumed to be equivalent to a 3806 K gray body with an emissivity of 0.97 as proposed by Null and Lozier (Ref. 6). The measured plasma intensity is compared with this standard intensity through the following relation:

$$\frac{F_\lambda^P}{F_\lambda^C} = \frac{\int_V \int_\Omega j_\lambda \, d\Omega dV}{\int_A \int_\Omega \epsilon B_\lambda \, d\Omega dA} \tag{3}$$

where F_λ^P is the plasma-emitted spectral flux incident on the phototube (W/μm), F_λ^C is the calibration spectral flux (W/μm), j_λ is the plasma emission coefficient (W/cm^3-μm-sr), ϵB_λ is the arc specific intensity (W/cm^2-μm-sr), Ω is the solid angle (sr), and V and A are the plasma volume and arc area, respectively.

Since the phototube voltage output E is proportional to the incident flux,

$$\frac{E^P}{E^C} = \frac{F_\lambda^P}{F_\lambda^C} \tag{4}$$

If one assumes an isotropic, homogeneous plasma and small viewing angles ($\cos\theta \doteq 1$), Eqs. (3) and (4) can be combined and simplified to

$$j_\lambda = \epsilon B_\lambda \frac{\int_A \Omega dA}{\int_V \Omega dV} \frac{E^P}{E^C} \tag{5}$$

The integrals in Eq. (5) must be evaluated for the particular geometry of the experimental setup. This was done for the present experiment and is detailed in Appendix C. The final result is simply

$$\frac{\int_A \Omega dA}{\int_V \Omega dV} = \frac{1}{\ell}$$

[4]Mole-Richardson Co., Hollywood, Calif.

where ℓ is the length of plasma being viewed. Thus the plasma intensity emitted (W/cm^2-μm-sr) is

$$I_\lambda = j_\lambda \ell = \epsilon B_\lambda \frac{E^P}{E^C} \qquad (6)$$

C. Results

The room temperature composition of the test gas was a mixture of 20% H_2 and 80% He, supplied by the Matheson Co., Inc., Cucamonga, Calif. A helium-rich mixture was used to raise the resultant plasma temperature, at a given shock speed, thus ensuring a large electron concentration. Profiles of the Hβ line were measured behind the reflected shock wave at incident shock speeds of 12 to 14 km/s, and behind the incident shock at speeds of 17 to 27 km/s. This represents plasma conditions of temperature and electron density of 11,800 to 15,600 K and 0.18×10^{17} to 0.57×10^{17} cm^{-3}, respectively.

Shown in Fig. 8 is a representative example of a set of phototube output oscillograms. These results are from the reflected shock region for an initial pressure of 66.6 N/m^2 (0.5 mm Hg) and an incident shock speed of 12.5 km/s. The radiative intensity of each slit is displayed as a function of time along with the output of a wide-band (visible) phototube viewing the test region. This phototube is generally used to indicate the arrival of the shock wave and the termination of the test at the arrival of the contact surface.

The spectral line intensity is seen to lag the radiation front detected by the wide-band tube. This result is at least partially due to the long response time of the 1P28 circuits. The traces do, however, reach an equilibrium level and indicate a constant-property test slug of at least 12 μs. At an initial pressure of 33.3 N/m^2 (0.25 mm Hg), the test times are approximately half as long; however, the traces still reach a plateau and remain constant for several microseconds.

Behind the incident shock, data were obtained at shock velocities of 17 to 20 km/s in 133.3 N/m^2 (1.0 mm Hg) and 21 to 27 km/s in 33.3 N/m^2 (0.25 mm Hg). An example of these data is shown in Fig. 9 for an initial pressure of 133.3 N/m^2 (1.0 mm Hg) and a shock velocity of 20.0 km/s. The indicated test time is 10 to 12 μs; the intensity falloff will be discussed in the next section. The test time for the 33.3-N/m^2 (0.25-mm Hg) data is estimated to be from 4 to 6 μs. In this case the "plateau" region was very short, on the order of 1 to 2 μs.

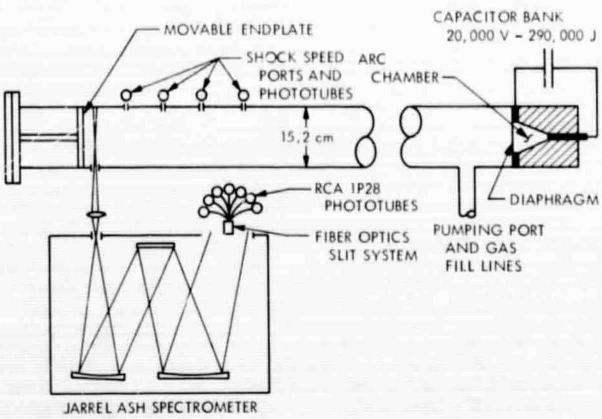

Fig. 6. Schematic of experimental setup showing JPL 15-cm arc-driven shock tube

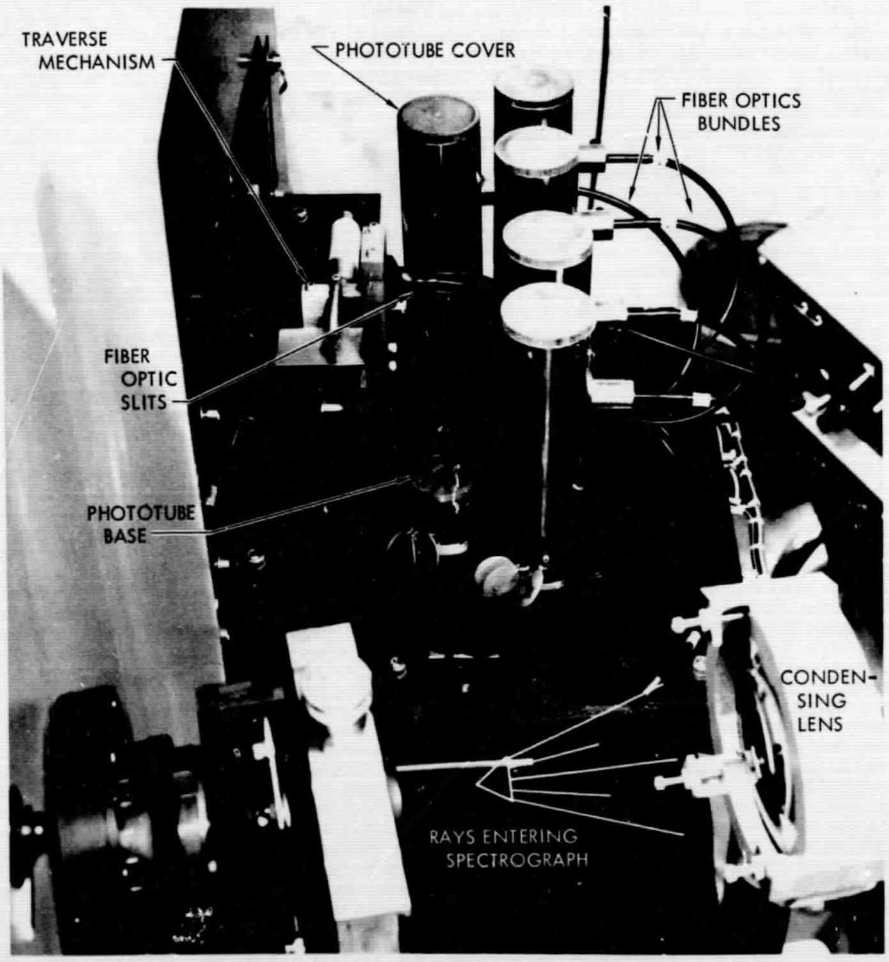

Fig. 7. Photograph of slit system and phototube positions on the spectrograph

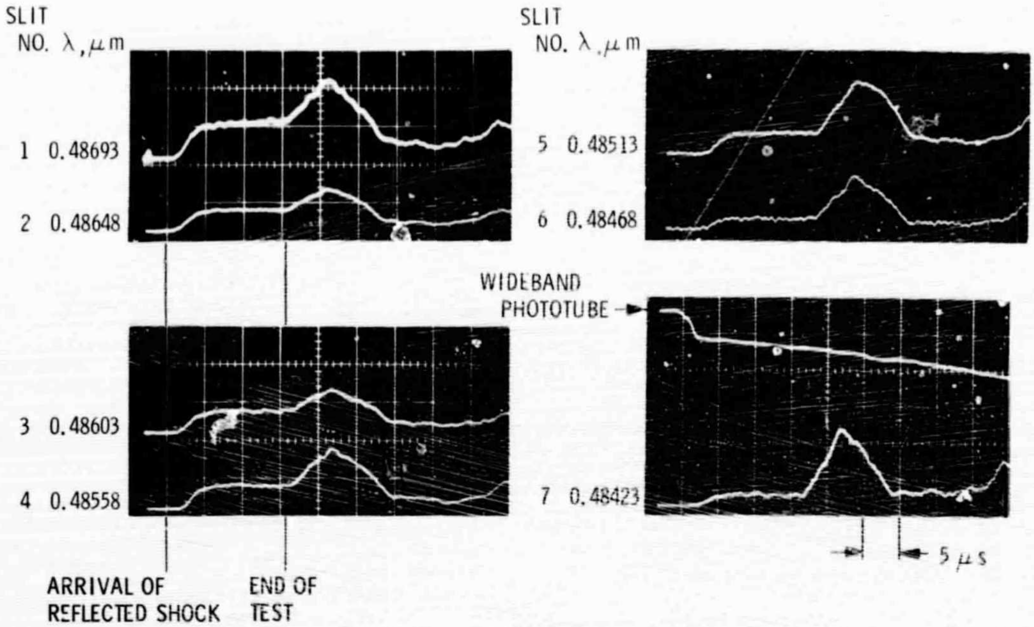

Fig. 8. Oscillograms of Hβ spectral intensity measurements, run 257, $P_1 = 66.6\ N/m^2$, $V_s = 12.5$ km/s

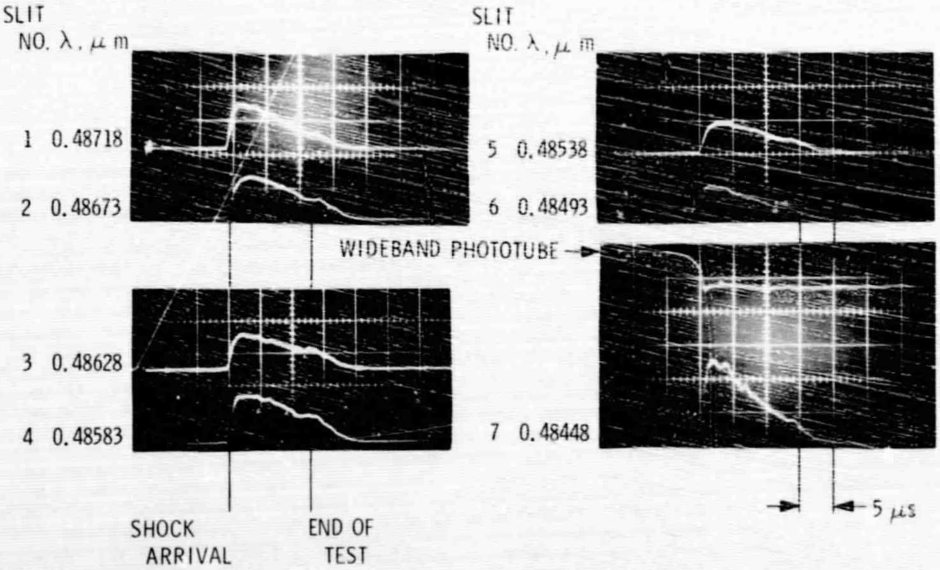

Fig. 9. Oscillograms of Hβ spectral intensity measurements, run 288, $P_1 = 133.3\ N/m^2$, $V_s = 20.0$ km/s

IV. DISCUSSION

In order to produce an equilibrium plasma in a test facility it is necessary, first, to have sufficient time to establish thermodynamic equilibrium, and, second, to have a large enough electron density to maintain it. According to Griem (Ref. 1, pp. 153), a hydrogen plasma of approximately 12,000 K and 10^{16} electrons/cm^3 requires about 3 μs to reach equilibrium. This is particle time, which is equivalent to 1/2 to 1/4 μs laboratory time (time as indicated on the oscilloscope traces). Thus at all conditions of the present experiment there is sufficient test time to allow the plasma to reach equilibrium within the test slug.

The second equilibrium criterion requires that the electron population be large enough to ensure that the number of excitation collisions (due primarily to electrons) is much larger than the number of de-excitation reactions due to spontaneous emission. The electron density required to maintain equilibrium at the temperatures of this experiment is 0.6×10^{16} cm^{-3}. The electron densities range from 4 to 10 times greater than this minimum value for the data to be presented.

It is therefore concluded that for the present experimental conditions, the plasma test slug should reach equilibrium in less than 1 μs (laboratory time) after the passage of the shock wave and remain in equilibrium throughout the test slug. The plasma properties behind the incident shock and the reflected shock should correspond to the conditions predicted by the conservation equations and equilibrium thermodynamics.

Presented in Figs. 10-12 are the results of the Hβ line intensity distribution measurements obtained for 12 shock tube runs. Fig. 10 presents reflected shock data and Figs. 11 and 12 are incident shock data. In each case the data are compared with the computed line intensity using the equilibrium plasma conditions corresponding to the measured shock speed and initial pressure of the run (the solid line), as computed using the JPL thermochemistry computer program (Ref. 7).

The dashed curves are least squares fit profiles which were determined by varying the electron density until the profile best matched the measured intensity. To do this required that the calculated profiles first be normalized to pass through the measured points. The normalization factor was chosen in such a way that the average deviation of the calculated profile from the measured points was zero. The electron density was then varied a few percent, and a new profile was calculated and compared with the measured points. This process was repeated until the sum of the squares of the average deviation was minimized. The final profile gave the measured electron density corresponding to the measured profile.

Without an additional experimental measurement, it is impossible to infer any other independent plasma property from these measurements. Since the overall magnitude of the line intensity is dependent on both the temperature and the atom number density, one must specify one of these in order to determine the other. It is observed, however, that the line intensity varies with the 10th or 12th power of temperature in this range of temperatures. Therefore a temperature variation of 2 or 3% will cause the intensity to vary 20 to 40%. Since the measured intensity is generally within 20% of the computed intensity and is never more than 50% (excluding run 293), it is possible to conclude from the data that the plasma temperature is within 5% of the computed temperature for all the runs examined.

Presented in Table 1 is a summary of 15 shock tube runs. The last column is a ratio of the best-fit measured electron density to the computed equilibrium electron density. In general, the electron density is within 20% of the computed value and on the average is about 10% low. The exception is run 293, which was the highest-speed run, with a shock velocity of 27 km/s. The indicated electron density is 40% below the computed value.

From the measured profile for run 293 in Fig. 12d, it can be seen that the measured intensity in the wings is a factor of 2 below the expected intensity. This is too large a difference to be attributed to experimental error. Although the test time was short (2.5 to 3 μs), it is long enough to establish equilibrium.

This discrepancy may be caused by a combination of two effects: the long rise time of the phototube circuits combined with radiative cooling of the gas. The gas may be reaching equilibrium in less than 1 μs behind the shock followed by radiative cooling. The phototube response would miss the equilibrium peak and catch up with the true signal some time later, after some cooling had taken place.

The fact that radiative cooling is an important phenomenon behind the incident shock can be demonstrated by a closer examination of run 288. In this case the radiative flux is high and the test time is long, so that the effect of cooling is emphasized. Reexamining the phototube outputs from run 288, shown in Fig. 9, it can be seen that the intensity rises to a peak level within 1-1/2 μs, then decreases slowly for 8 to 10 μs until the arrival of the contact surface. The line shape was measured just prior to the arrival of the contact surface, and the results are presented in Fig. 12a along with the equilibrium shape. The line intensity is over 50% lower than the equilibrium line intensity.

In order to determine the thermodynamic conditions corresponding to this new line shape, the least squares fit technique was again used. In this case both the temperature and electron density were varied until the computed line shape fitted the experimental measurements. To do this required an assumption regarding the process by which the gas went from one point to the other. To simplify the analysis, two limiting cases were used: flow at constant density (corresponding to hypersonic cooling) and flow at constant pressure (corresponding to incompressible cooling). In each case the pressure or density was held constant at the equilibrium value behind the shock, and the temperature and electron density was varied to determine the best-fit profile. The results are shown in Table 2.

The measured electron density in column 2 is that obtained from the best-fit profile; the equilibrium electron density corresponds to the temperature in column 1 and the equilibrium density or pressure behind the shock. The indicated temperature reduction is something between 10 and 20%, depending on the flow process. In comparing the measured and equilibrium electron density, it is apparent that the final thermodynamic state corresponds very nearly to an equilibrium condition. Thus the flow seems to be changing conditions while remaining in equilibrium. This is consistent with a cooling phenomenon as opposed to a nonequilibrium phenomenon such as de-excitation due to radiative decay.

The fact that radiative cooling can be important at these conditions is demonstrated by comparing the radiative flux emitted by the test slug to the energy convected through the shock wave into the test slug. This ratio, called the radiative cooling parameter (Ref. 8), is

$$\Gamma = \frac{F_{rad}}{1/2\,\rho_1 V_s^3 A} \qquad (7)$$

where F_{rad} is the isothermal radiative flux emitted by the test slug, ρ_1 is the density before the shock, V_s the shock velocity, and A is the frontal area of the test slug. Radiative cooling is important whenever this parameter is near 0.1 or is larger. Shown in Fig. 13 is Γ computed for the present experimental conditions of the incident shock cases. All runs above 20 km/s are greatly affected by radiative cooling. In fact, on several of the 18-km/s runs, with initial pressure 133.3 N/m^2 (1.0 mm Hg), a small amount of cooling was noticed.

It appears that run 293, with a Γ greater than 0.2, would have a great deal of cooling. Thus the plasma probably cooled to a lower temperature and electron density within the time it took the phototube to respond, as proposed above.

Table 1. Summary of shock tube runs

Run No.	Configuration	P_1, N/m^2 (mm Hg)	V_s, (km/s)	T, K	Ne/Ne (ideal)
245	RS	33.3 (0.25)	14.0	13,825	0.992
252		33.3 (0.25)	12.0	12,265	0.935
253		33.3 (0.25)	12.5	12,610	0.790
257		66.6 (0.50)	11.0	12,050	0.827
259	RS	66.6 (0.50)	12.9	13,425	0.881
283	IS	133.3 (1.0)	17.0	11,870	1.138
284		133.3 (1.0)	18.05	12,540	0.935
285		133.3 (1.0)	18.8	13,000	0.842
286		133.3 (1.0)	18.3	12,690	1.013
287		133.3 (1.0)	18.3	12,690	0.841
288		133.3 (1.0)	20.0	13,710	0.779
290		33.3 (0.25)	21.8	13,690	1.19
291		33.3 (0.25)	21.4	13,460	0.947
292		33.3 (0.25)	24.4	15,630	0.880
293	IS	33.3 (0.25)	27.0	17,690	0.598

RS = Reflected shock.
IS = Incident shock.

Table 2. Theoretical and measured conditions behind the incident shock, V_s = 20.0 km/s, P_1 = 133.3 N/m^2

Conditions	T, K	Measured Ne, $1/cm^3$	Equilibrium Ne, $1/cm^3$	Temperature reduction, %
Theoretical equilibrium conditions behind incident shock	13,710	–	0.465×10^{17}	–
Measured electron density immediately behind incident shock	–	0.362×10^{17}	–	–
Measured conditions 20 cm behind incident shock, assuming constant density flow	12,463	0.275×10^{17}	0.288×10^{17}	11.0
Measured conditions 20 cm behind incident shock, assuming constant pressure flow	11,677	0.275×10^{17}	0.270×10^{17}	17.5

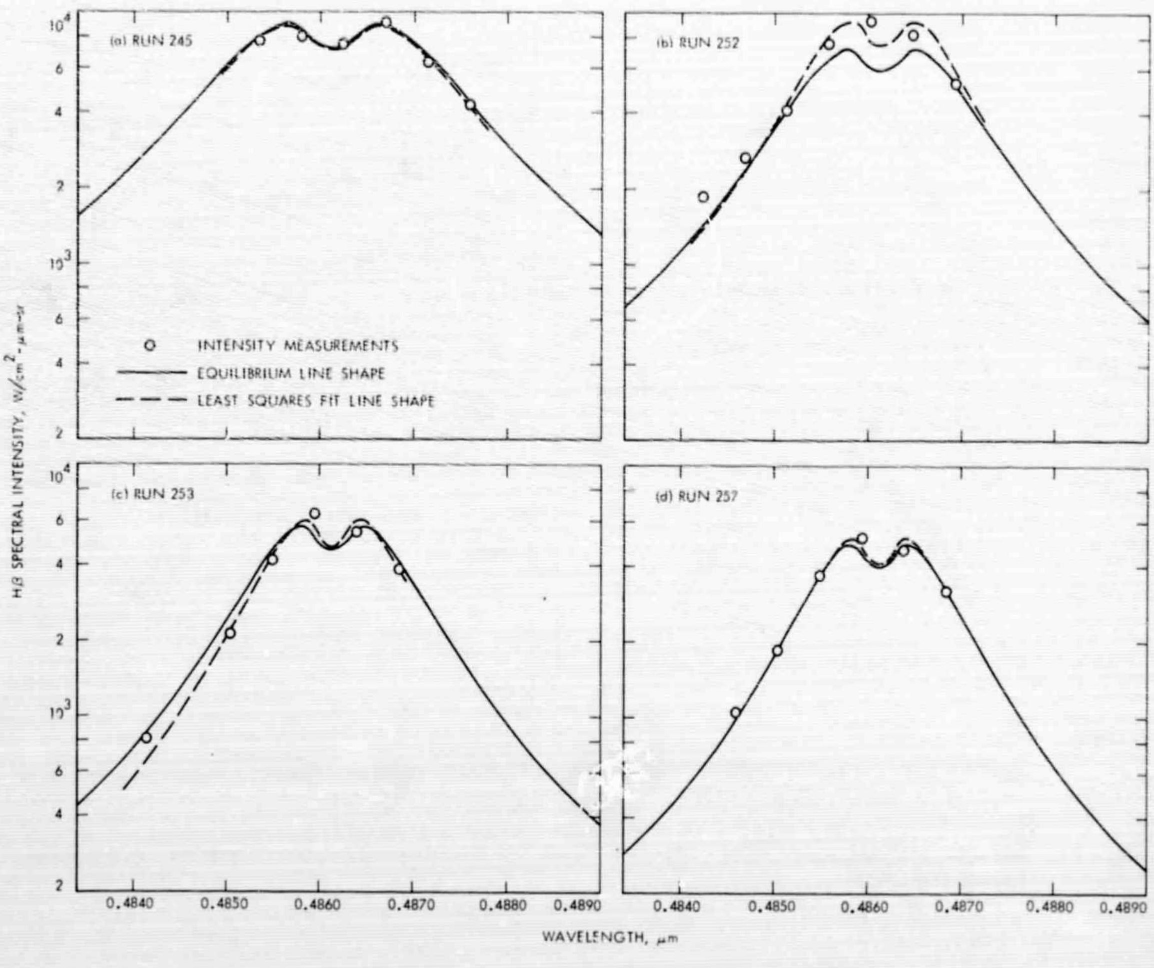

Fig. 10. Hβ spectral intensity data compared with the theoretical profile, reflected shock case

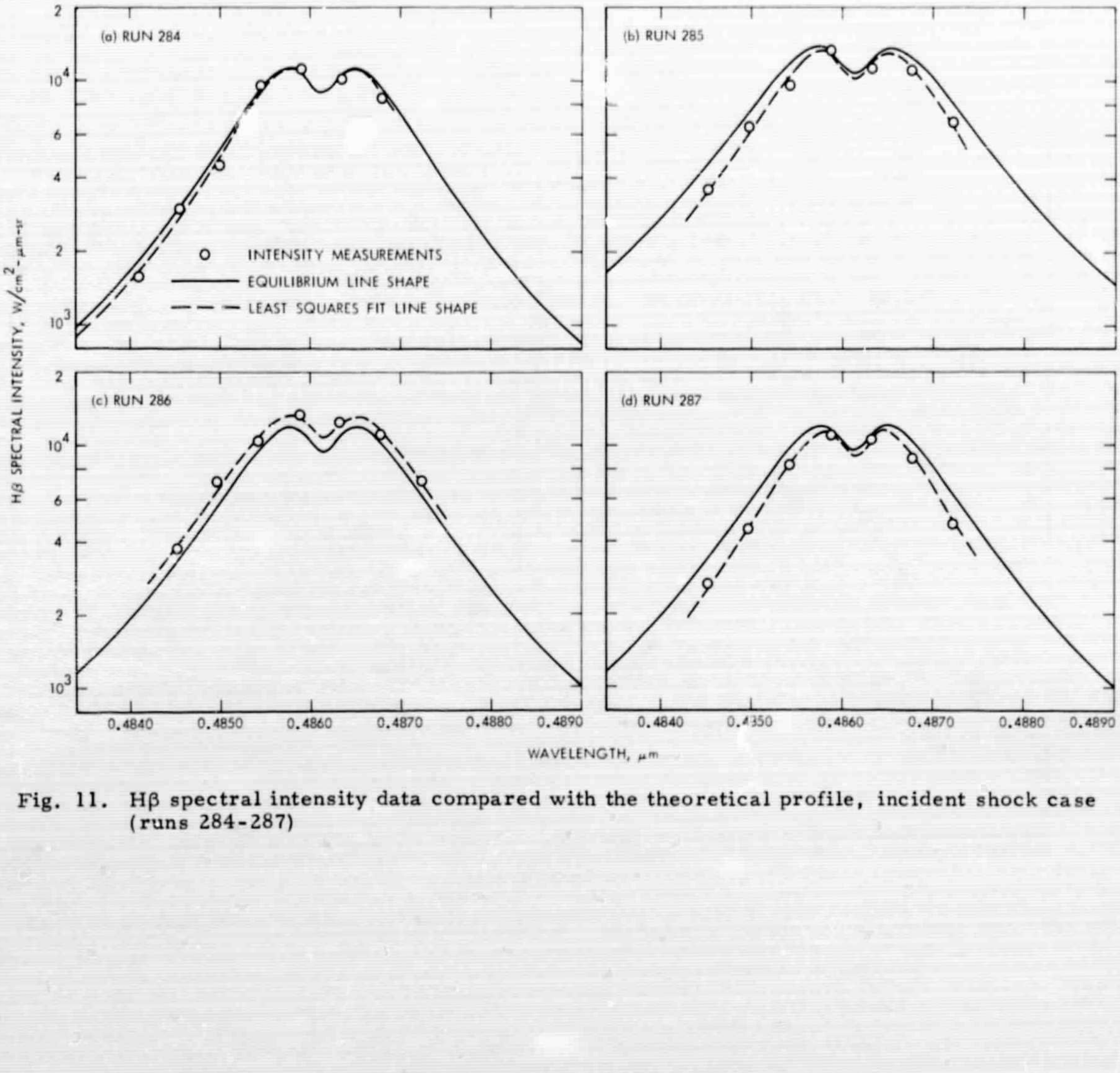

Fig. 11. Hβ spectral intensity data compared with the theoretical profile, incident shock case (runs 284-287)

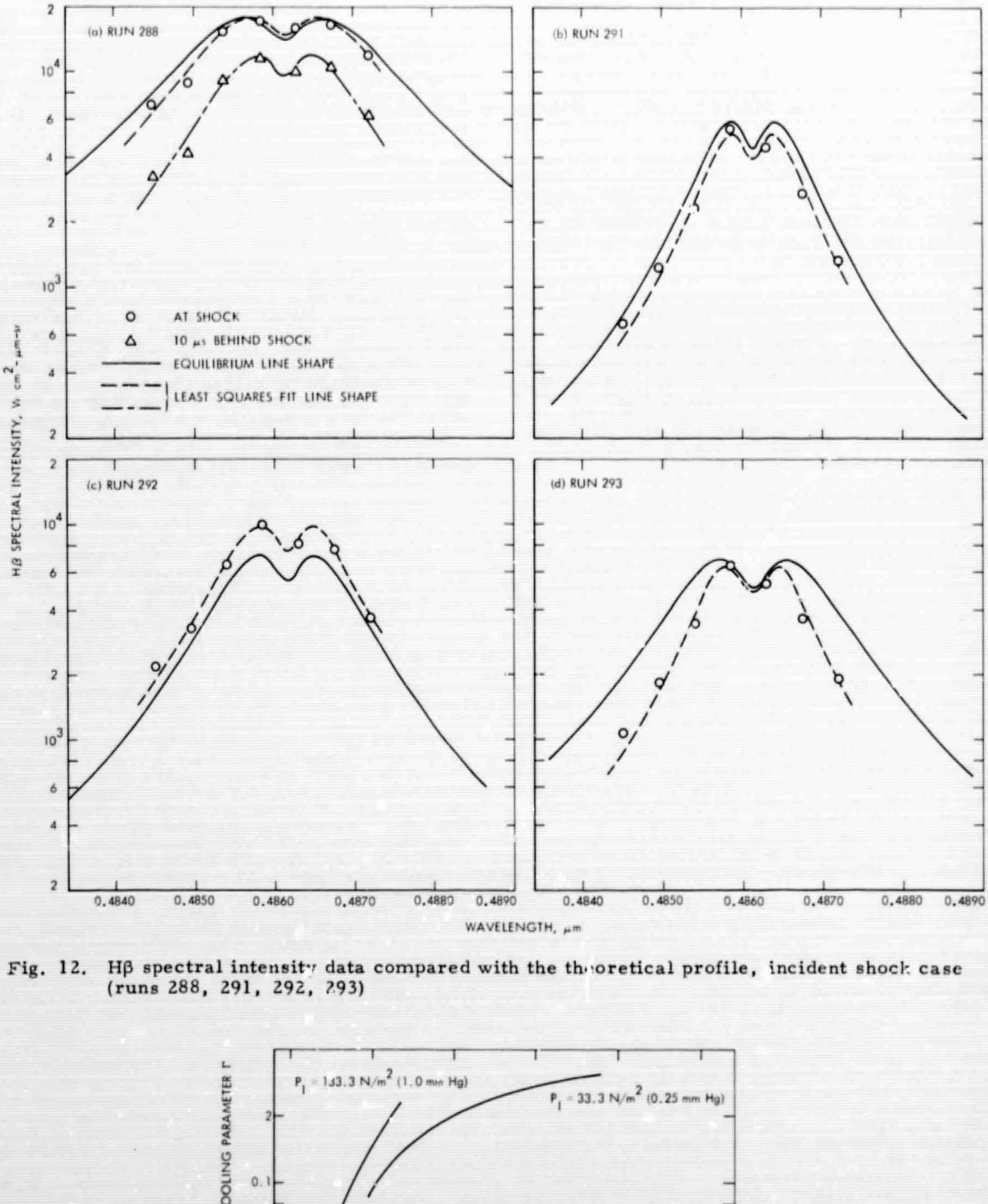

Fig. 12. Hβ spectral intensity data compared with the theoretical profile, incident shock case (runs 288, 291, 292, 293)

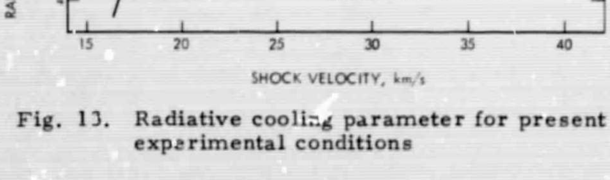

Fig. 13. Radiative cooling parameter for present experimental conditions

V. CONCLUSIONS

A fiber optics slit system has been demonstrated to be a useful technique for measuring the shape and absolute magnitude of the Hβ line intensity emitted by a transient plasma. Using these data one may obtain the time-resolved electron density of the plasma and, with some knowledge of the pressure or density, the temperature as well. The technique is simpler and much more direct than other methods which rely on photographic processes used in conjunction with high-speed shutters or rotating mirrors to obtain time resolution.

The problems associated with the fiber optics slit system have been analyzed and found to be manageable. The slit function has been computed for several cases, and it has been shown that asymmetries in the slit function have a negligible effect on the intensity measurement. The numerical aperture was found to be sufficiently large to allow all the light falling on the slits to be transmitted to the phototubes.

The Hβ line intensity profile has been measured in the shock tube for several different plasma conditions. In all but one case, the measured intensity agreed to within 20 to 50% of the computed intensity using equilibrium shock tube thermodynamic conditions. In terms of plasma conditions, the temperature was found to be within a few percent of the predicted temperature, and the electron density within 10 to 20% of the predicted electron density.

Radiative cooling was found to be an important process behind the incident shock at shock speeds of 20 km/s and above. For one run, the measured temperature dropped 10 to 20% through the test slug. Since the measured electron density indicated that thermodynamic equilibrium existed throughout the test slug, it was concluded that radiative cooling was responsible for the change in flow properties. A calculation of the radiative cooling parameter verified the importance of cooling at these conditions.

REFERENCES

1. Griem, H. R., Plasma Spectroscopy, McGraw-Hill, Inc., 1964.

2. Griem, H. R., Kolb, A. C., and Shen, K. Y., "Stark Broadening of Hydrogen Lines in a Plasma," Phys. Rev., Vol. 116, p. 4, 1959.

3. Hill, R. A., and Gerardo, J. B., "Stark Broadening of $H\beta$, $H\gamma$, and $H\delta$: An Experimental Study," Phys. Rev., Vol. 162, p. 45, 1967.

4. Menard, W. A., "A Higher Performance Electric-Arc-Driven Shock Tube," JPL Quarterly Technical Review, Vol. 1, p. 17, April 1971.

5. Menard, W. A., and Thomas, G. M., "Radiation Measurement Techniques," Technical Report 32-975. Jet Propulsion Laboratory, Pasadena, Calif., 1966.

6. Null, M. R., and Lozier, W. W., "The Carbon Arc as a Radiation Standard," Temperature. Its Measurement and Control in Science and Industry, Vol. III, Part 1. Basic Concepts, Standards, and Methods, p. 551. Reinhold Publishing Corp., Chapman & Hall, Ltd., London.

7. Horton, T. E., and Menard, W. A., A Program for Computing Shock Tube Gasdynamic Properties, Technical Report 32-1350. Jet Propulsion Laboratory, Pasadena, Calif., Jan. 15, 1969.

8. Goulard, R., "The Radiative Transfer Problem in Detached Shock Layers," AIAA Paper 63-452. Presented at the AIAA Conference on Physics of Entry into Planetary Atmospheres, American Institute of Aeronautics and Astronautics, 1963.

APPENDIX A

SLIT FUNCTION FOR CIRCULAR FIBER-FILLED SLITS

The slit function $f(\lambda)$ can be defined as the percentage of the entrance slit image transmitted through the exit slit. We will assume a rectangular entrance slit of width $\Delta\lambda^*$ and a circular fiber-filled exit slit of width $\Delta\lambda$, as shown in Fig. A-1. The center of the exit slit is at λ_0 and the position (center) of the entrance slit image is λ. The computation of the slit function consists simply of adding the area of the circular fibers within $\Delta\lambda^*$ for each position λ of the entrance slit image,

$$f(\lambda) = \frac{\text{Area of fibers within } \Delta\lambda^*}{\text{Area of } \Delta\lambda^*}$$

Alternatively, one may compute the slit function for a vanishingly thin entrance slit image $f'(\lambda)$. This is much simpler since it consists of computing the length of a line at λ falling within the circular fibers divided by the total length of the line. The slit function for an entrance slit of width $\Delta\lambda^*$ is then found[5] by averaging about λ, i.e.,

$$f(\lambda) = \frac{1}{\Delta\lambda^*}\int_{\lambda-\Delta\lambda^*/2}^{\lambda+\Delta\lambda^*/2} f'(\xi)\,d\xi \qquad \text{(A-1)}$$

at numerous points across the slit.

Following this technique, and noting that the slit function is symmetric about λ_0 for the non-overlapping configuration shown in Fig. A-1,

$$f'(\lambda) = \begin{cases} \left[1-\left(\dfrac{2(\lambda-\lambda_0)}{d}\right)^2\right]^{1/2} & \text{for } \lambda_0 \le \lambda \le d/2 \\ \left[1-\left(\dfrac{2(\lambda-\lambda_0-d)}{d}\right)^2\right]^{1/2} & \text{for } d/2 \le \lambda \le \dfrac{3d}{2} \end{cases} \qquad \text{(A-2)}$$

Performing the integration indicated in Eq. (A-1), one obtains the slit function for any entrance slit width $\Delta\lambda^*$. Results are shown in Fig. A-2 for $\Delta\lambda^* = 0$, $\Delta\lambda^* = 1/8\,\Delta\lambda$, and $\Delta\lambda^* = 1/4\,\Delta\lambda$.

Similar results can be obtained for other fiber spacing. In the case of overlapping rows, there are three functions defining $f'(\lambda)$,

$$f'(\lambda) = \begin{cases} \left[1-\left(\dfrac{2(\lambda-\lambda_0)}{d}\right)^2\right]^{1/2} & \text{for } \lambda_0 \le \lambda \le (\sqrt{3}-1)\dfrac{d}{2} \\ \left[1-\left(\dfrac{2(\lambda-\lambda_0)}{d}\right)^2\right]^{1/2} + \left[1-\left(\dfrac{2(\lambda-\lambda_0-\frac{\sqrt{3}}{2}d)}{d}\right)^2\right]^{1/2} & \text{for } (\sqrt{3}-1)\dfrac{d}{2} \le \lambda \le \dfrac{d}{2} \\ \left[1-\left(\dfrac{2(\lambda-\lambda_0-\frac{\sqrt{3}}{2}d)}{d}\right)^2\right]^{1/2} & \text{for } \dfrac{d}{2} \le \lambda \le (\sqrt{3}+1)\dfrac{d}{2} \end{cases} \qquad \text{(A-3)}$$

The results for this case for $\Delta\lambda^* = 1/4\,\Delta\lambda$ are shown in Fig. 4 of this report.

[5] As suggested by Wesley Menard, Jet Propulsion Laboratory, Pasadena, California.

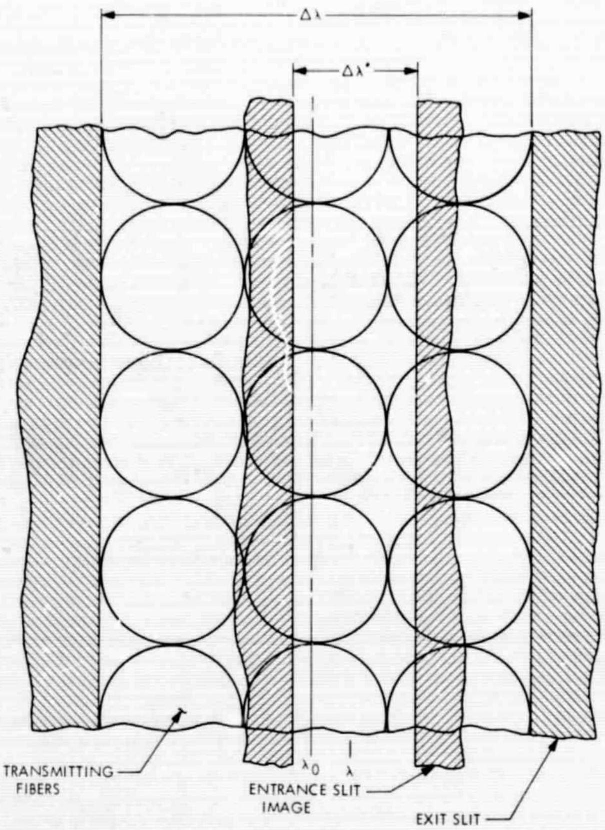

Fig. A-1. Exit slit model for computing slit function

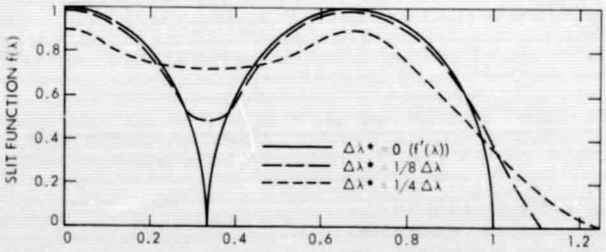

Fig. A-2. Slit function for nonoverlapping fibers

APPENDIX B

THE EFFECT OF SLIT FUNCTION ASYMMETRY ON MEASURED INTENSITY

In order to understand the importance of slit function asymmetry, a simplified model of a slit function was constructed, shown in Fig. B-1. A nondimensional wavelength

$$\xi = \frac{2(\lambda - \lambda_0)}{\Delta\lambda} \tag{B-1}$$

is used where λ_0 is the center of the exit slit and $\Delta\lambda$ is the exit slit width. The intensity I_λ is nondimensionalized by the intensity at the slit center I_0, which is the value we wish to measure. The slit function is assumed to be a linear function of ξ,

$$f(\xi) = 1 + A\xi \tag{B-2}$$

and the intensity is assumed to be linear across the slit,

$$\frac{I_\lambda}{I_0} = 1 + B\xi \tag{B-3}$$

where

$$A = \frac{df}{d\xi}$$

$$B = \frac{d\frac{I_\lambda}{I_0}}{d\xi}$$

The measured intensity $\tilde{I}_\lambda$ is

$$\frac{\tilde{I}_\lambda}{I_0} = \frac{1}{2}\int_{-1}^{1} \frac{I_\lambda}{I_0} f(\xi)\, d\xi$$

$$= 1 + \frac{AB}{3} \tag{B-4}$$

Thus, we see that the error in the measured intensity is one-third the product of the nondimensional slopes of the slit function and the intensity distribution. If either slope is zero, the error is zero as one would intuitively expect.

The average slope of the measured slit functions is never greater than 0.15; thus, as a conservative estimate, choose

$$A = 0.15$$

The maximum slope of the intensity is found as follows. For a dispersion-shaped line, the intensity distribution is

$$I_\lambda = I_{MAX} \frac{b^2}{(\lambda - \lambda_0)^2 + b^2} \tag{B-5}$$

where I_{MAX} is the line center intensity and b is the line (half) half-width. The slope is

$$\frac{dI_\lambda}{d_\lambda} = I_{MAX} \frac{2b^2(\lambda - \lambda_0)}{\left[(\lambda - \lambda_0)^2 + b^2\right]^2} \tag{B-6}$$

The maximum slope is found by setting

$$\frac{d}{d_\lambda}\left(\frac{dI_\lambda}{d_\lambda}\right) = 0$$

which occurs at

$$\lambda - \lambda_0 = \frac{b}{\sqrt{3}} \tag{B-7}$$

The maximum slope is then, substituting Eq. (B-7) into Eq. (B-6),

$$\left(\frac{dI_\lambda}{d_\lambda}\right)_{MAX} = \frac{9}{8\sqrt{3}} \frac{I_{MAX}}{b} \tag{B-8}$$

Nondimensionalizing, we have

$$\frac{d\frac{I_\lambda}{I_0}}{d\xi} = \frac{9}{16\sqrt{3}} \frac{I_{MAX}}{I_0} \frac{\Delta\lambda}{b} \tag{B-9}$$

Now by evaluating Eq. (B-5) at $\lambda - \lambda_0 = b/\sqrt{3}$, we find the intensity at the point of maximum slope,

$$I_0 = \frac{3}{4} I_{MAX}$$

Thus,

$$\frac{d\frac{I_\lambda}{I_0}}{d\xi} = \frac{3}{4\sqrt{3}} \frac{\Delta\lambda}{b} \tag{B-10}$$

The exit slit width is $\Delta\lambda = 0.18$ nm, and the minimum line (half) half-width which could be considered is $b = 0.5$ nm. Therefore,

$$B = \left(\frac{\frac{dI_\lambda}{I_0}}{d\xi} \right)_{MAX} = 0.156$$

Substituting into Eq. (4B), we obtain

$$\frac{\tilde{I}_\lambda}{I_0} = 1.00778$$

The maximum error which could be attributed to slit asymmetry is less than 1%.

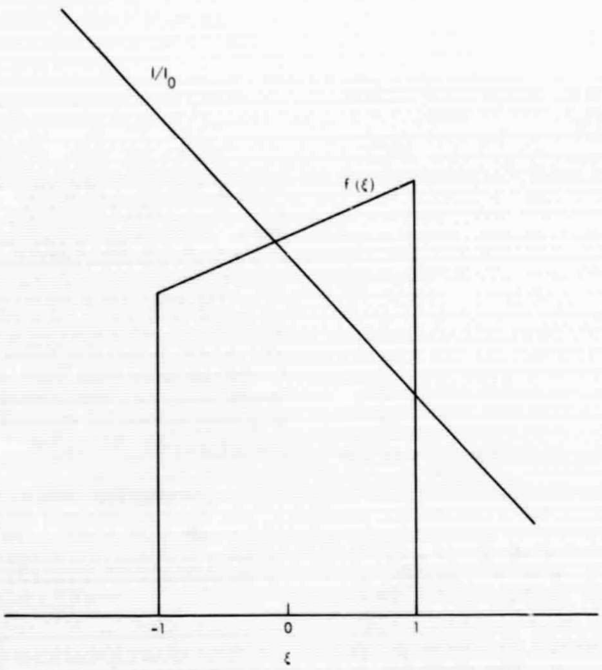

Fig. B-1. Slit function model used to determine the effect of symmetries

APPENDIX C

EVALUATION OF VIEW FACTOR INTEGRAL

The amount of radiative flux passing through the spectrograph entrance slit due to the emission of an optically thin gaseous source, shown in Fig. C-1, is

$$F_\lambda = \int_V \int_\Omega j_\lambda \, d\Omega \, dV \qquad \text{(C-1)}$$

where F_λ is the specific flux in watts/micrometer, j_λ is the emission coefficient of the gas, Ω is the solid angle in steradians, and V is the radiating volume being viewed by the spectrograph. For an isotropic, homogeneous gas (j_λ independent of direction and position) Eq. (C-1) becomes

$$F_\lambda = j_\lambda \int_V \int_\Omega d\Omega \, dV$$

$$= j_\lambda \int_z \int_y \int_x \Omega \, dx \, dy \, dz \qquad \text{(C-2)}$$

In general, Ω is a function of x, y, and z. However, for small angles, Ω will be constant from $x = 0$ to $x = x_1$ as shown in Fig. C-2. The point x_1 is the position of the inside limiting ray shown in Fig. C-1. From the inside limiting ray x_1 to the outside limiting ray x_2, the value of Ω drops linearly to zero. Thus, the integral in Eq. (C-2) becomes

$$\int_z \int_y \int_x \Omega(x, y, z) \, dx \, dy \, dz$$

$$= 4 \int_z \Omega(0, 0, z) x^*(z) y^*(z) \, dz$$

where

$$x^*(z) = (x_1 + x_2)/2 \quad \text{and} \quad y^*(z) = (y_1 + y_2)/2.$$

Let

$$\Omega(z) = \Omega(0, 0, z)$$

$$A(z) = 4x^*(z)y^*(z)$$

then

$$F_\lambda = j_\lambda \int_z \Omega(z) A(z) \, dz \qquad \text{(C-3)}$$

We will evaluate Eq. (C-3) for the case of rectangular slits where

$$y^*(1) = \delta << x^*(1)$$

In this case, there are four regions in which $\Omega(z)$ and $A(z)$ have a different functional relationship with z. In each region, however, we need evaluate Ω only along the z-axis.

Consider the view of the x-z plane shown in Fig. C-3. In regions 1 and 4 the solid angle of any point along the z-axis is limited by the spectrograph entrance slit. In regions 2 and 3 the limit becomes the optical stops on the lens in the x-z plane, but in the y-z plane (refer to Fig. C-1) the entrance slit is still the limiting stop.

Defining the solid angle at any point as

$$\Omega = \frac{\text{Area of lens subtended by limiting rays}}{(\text{Distance from lens})^2}$$

the functional form of $\Omega(z)$ in the four regions is found to be

1 $\quad \Omega(z) = \dfrac{4\delta x^*(1)}{(1-z)^2}$

2 $\quad \Omega(z) = \dfrac{4\delta}{z(1-z)}$

3 $\quad \Omega(z) = \dfrac{4\delta}{z(1-z)}$

4 $\quad \Omega(z) = \dfrac{4\delta x^*(1)}{(z-1)^2}$

The midpoints of the limiting rays, $x^*(z)$ and $y^*(z)$ are, for the four regions,

1	$x^*(z) = 1-z$	$y^*(z) = 1-z$
2	$x^*(z) = x^*(1)z$	$y^*(z) = 1-z$
3	$x^*(z) = x^*(1)z$	$y^*(z) = z-1$
4	$x^*(z) = z-1$	$y^*(z) = z-1$

Finally, for $\Omega(z) \cdot A(z)$, where $A(z) = 4x^*(z) \cdot y^*(z)$, ① $\Omega(z)A(z) = 16\delta x^*(1)$

② $\Omega(z)A(z) = 16\delta x^*(1)$

③ $\Omega(z)A(z) = 16\delta x^*(1)$

④ $\Omega(z)A(z) = 16\delta x^*(1)$

Thus, we see that $\Omega(z) \cdot A(z)$ is constant over all z and the integral

$$\int \Omega(z)A(z)\, dz = \ell\,\Omega(1)A(1)$$

so that the flux becomes

$$F_\lambda = j_\lambda \ell\,\Omega(1)A(1)$$

where ℓ is the length of the radiating source.

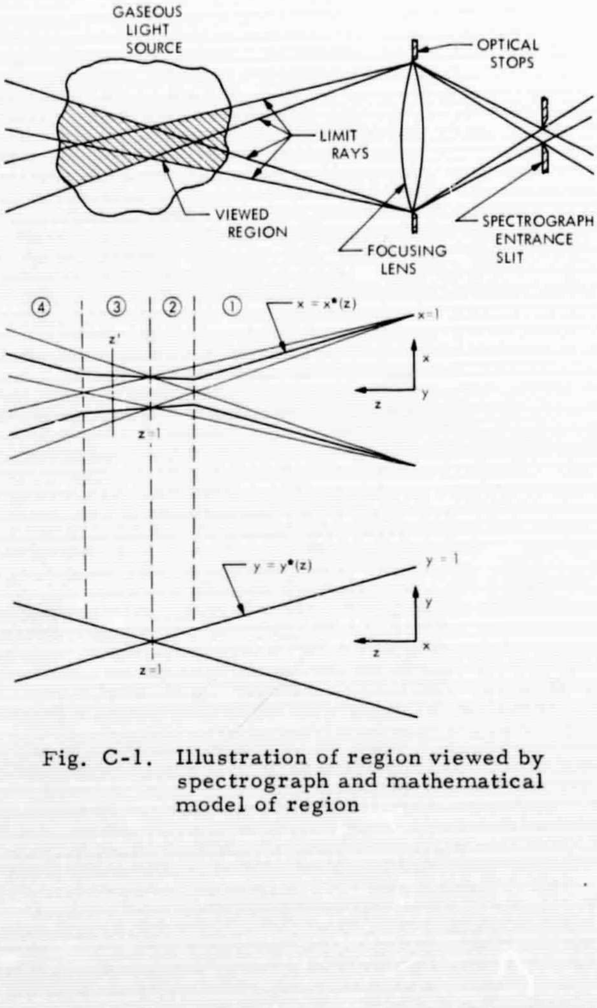

Fig. C-1. Illustration of region viewed by spectrograph and mathematical model of region

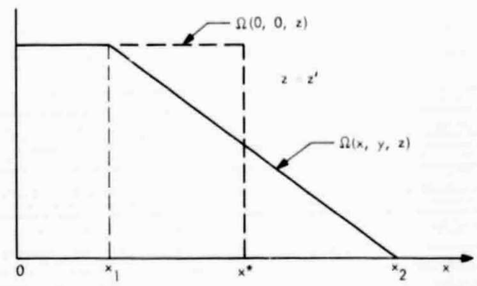

Fig. C-2. Description of integration scheme

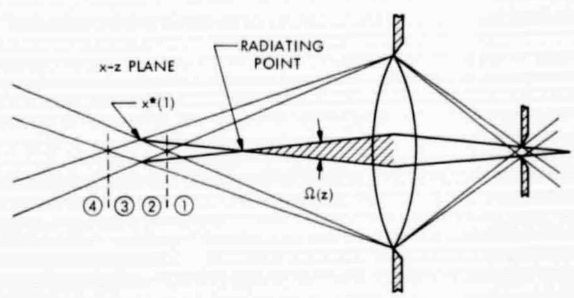

Fig. C-3. Description of solid angle, $\Omega(z)$, at arbitrary point

NASA — JPL — Coml., L.A., Calif.